Hindawi
International Transactions on Electrical Energy Systems
Volume 2022, Article ID 3525601, 20 pages
https://doi.org/10.1155/2022/3525601

Research Article

Introducing MRAC-PSS-VI to Increase Small-Signal Stability of the Power System after Wind Power Integration

Ping He, Mingming Zheng, Haoran Jin, Zhijie Gong, and Jie Dong

College of Electric and Information Engineering, Zhengzhou University of Light Industry, Zhengzhou, Henan, China

Correspondence should be addressed to Ping He; hplkz@126.com

Received 30 September 2021; Revised 29 November 2021; Accepted 20 December 2021; Published 31 January 2022

Academic Editor: Youssef Errami

With the gradual increase of wind power penetration in the power system, the impact of wind farm on system stability is becoming more significant. This study designs the power system stabilizer (PSS) based on the model reference adaptive control (MRAC) method and virtual impedance (VI) control strategy. Then, the active power difference of the doubly fed induction generator (DFIG) is selected as input signal of MRAC-PSS-VI. The small-signal stability of the power system with the DFIG is enhanced by installing MRAC-PSS-VI on the rotor side control (RSC) control link. The controller model is built in DigSILENT/PowerFactory. The improvement effect of the controller on the low-frequency oscillation (LFO) characteristics of the power system is verified by using eigenvalue analysis and the time domain simulation method under different transmission powers of the tie line and different installed positions of the DFIG.

1. Introduction

While wind power is used as potential source of electricity, the development of wind energy is increasing rapidly around the world. During wind power conversion, the doubly fed induction generator (DFIG) has the most important position in electrical machine, thanks to the DFIG that has an advantage in low power rating of the rotor side converter (RSC), high power capacity in both subsynchronous and supersynchronous operating conditions, and low power rotor side easy to control. In addition, the DFIG can realize constant frequency power generation under different wind speed conditions. For good measure, decoupled power injection capability and harmonic suppression capability of the DFIG are similar to the conventional synchronous generator.

A variety of control strategies of the DFIG are presented in published studies. Pena et al. [1] illustrated a stator and rotor field-oriented vector control strategy, while the direct torque control scheme (DTC), direct power control strategy (DPC), and direct flux control strategy are illustrated in [2–5]. All of these control schemes require coordinate axis transformation of rotor position and control of velocity information. In order to stabilize the oscillation of the power system, Surinkaew and Ngamroo [6] proposed a coordinated control method between the DFIG and synchronous generator while installed the power oscillation damper (POD) and power system stabilizer (PSS), respectively. In the study by Rahim and Habiballah [7], the DFIG rotor voltage control for system dynamic performance enhancement is proposed. The POD equipped with the DFIG based on a phase lead compensation is able to improve the network damping. In recent years, many literatures are devoted to researching the additional damping control strategy of the DFIG. In the study by Hughes et al. [8], the PSS of wind turbine with the DFIG is proposed, which proves that the PSS can significantly affect the contribution of wind farm based on the DFIG to power grid damping. The feasibility of the DFIG providing additional damping is investigated, and the DFIG wind generators installing the PSS are synchronously applied to increase damping levels of a multimachine power system [9]. Mohamed et al. [10] pointed out the influence of the DFIG operation and control on rotor angle stability and proposed a PSS with the DFIG reactive power as input signal to improve rotor angle stability of the system. Surinkaew and Ngamroo [11] proposed a two-level stratified strategy

consisting of wide area centralized and local controls of POD installed with the DFIG wind power turbine, and the PSS has been proposed for robust power oscillation damping. But all these control schemes do not take the output impedance of the PSS into account. Virtual impedance (VI) control method is very common in microgrid, but it has not been applied in the PSS controller. In order to adjust the output impedance of the PSS, this work introduces the virtual impedance method. The positive sequence virtual impedance can be introduced to improve the power distribution effect of the distributed generators (DGs), and the negative sequence VI is introduced to make up for the voltage drop because of the negative sequence current on the line impedance and to reduce the negative sequence circulating current [12]. Pham and Lee [13] proposed a heightened DG-VI controller to supply harmonic voltage compensation and accurate power harmonic sharing of microgrid. Qian et al. [14] proposed an adaptive VI control strategy considering both power quality and stability constraints based on the small-signal model of the global positioning system (GPS) microgrid. It is well known that the PSS is an additional damping controller used to suppress LFO in the power system. In order to facilitate the application of the PSS, the MRAC method is introduced in this work. Coman and Boldisor [15] studied the adjustment mechanism of MRAC by using a gradient method (Massachusetts Institute of Technology (MIT) rule) or using a stability theory (Lyapunov method). Sharma and Kumar Palwalia [16] proposed a modified proportion integration differentiation (PID) control using an adaptive controller. Hung et al. [17] presented MRAC compared to cascade PID control for the purpose of evaluating their performance. In the study by Mohamed et al. [18], the applicability of sensorless speed estimation technology based on different model reference adaptive systems (MRAS) in the brushless doubly fed reluctance generator is discussed.

Although the oscillation damping characteristics have been investigated, there are still several important problems with regard to improving LFO characteristics in a power system with wind power integrated to be solved. With the gradual increase of wind power penetration in the power system, the impact of wind farm on system stability gets more significant. The objective of this work is to ensure the small-signal stability of a power system effectively with plentiful integration of wind farms generation. The main contributions of this work are summarized as follows:

(a) The PSS controller is improved based on the VI control method

(b) MRAC method is used to optimize the control of the designed PSS-VI

(c) The reference model of MRAC is designed by the TLS-ESPRIT method and regional pole assignment method

(d) Eigenvalue analysis method and time domain simulations method are employed to estimate the effects of heightening the stability after MRAC-PSS-VI is installed in the DFIG

This study is structured as follows. The mathematical model of MRAC and PSS-VI is expounded in Section 2. The mathematical model of the DFIG, the DFIG-MRAC-PSS-VI installation location, and the small-signal stability analysis model are given in Section 3. Finally, the effectiveness of the designed controller is verified by using the eigenvalue analysis method and time domain simulation method through a four-machine system, and some conclusions are given at the end of the study.

2. MRAC-PSS-VI Modeling

2.1. PSS-VI Model. The PSS is an auxiliary controller widely used in excitation control. The PSS can provide a control signal which includes a phase compensation through AVR to the excitation system in order to increase the system damping and obtain the damping effect on power oscillations. Figure 1 shows the block diagram of the single-input PSS used in the simulations of this study.

In the inverter, in order to decrease the cost of network construction and line loss, the virtual impedance can be introduced to replace the series inductance to make the inverter line impedance inductive. Based on this background, this study proposes that virtual impedance can be introduced to the power system stabilizer to adjust its output impedance without affecting its regulation effect.

The controller parameters not only directly affect the output impedance but also determine the rapidity and stability of the system. Therefore, the design of virtual impedance based on the controller parameters should take both factors into account, which will lead to a smaller design range of the controller parameters. Thus, this study proposes the control strategy of adding an impedance loop to the PSS control loop, which is used to adjust the PSS output impedance without affecting the regulation effect of the PSS.

PSS-VI output impedance is synthesized by selecting the reasonable virtual impedance and PSS output impedance, and then, the properties of PSS impedance are changed to improve the stability of the system. Figure 2 shows the vector diagram representation of virtual impedance. It can be seen from Figure 2 that the phase angle of PSS-VI output impedance will change when the virtual impedance is changed, so the PSS-VI output impedance can be regulated by changing the virtual impedance modulus value, while ensuring that the controller has a good unit step response.

The block diagram of the PSS-VI is shown in Figure 3.

PSS-VI input signal which can be selected rotor speed, voltage, current, or frequency has a great impact on the performance of the controller. Residual analysis is the most common method of signal selection. The input signal of the virtual impedance link adapts the filtering signal to ensure this link is not affected by the clutter of the PSS input signal.

2.2. Mathematical Model of MRAC. MRAC is designed based on Lyapunov theory and Barbalet's lemma to ensure stability and convergence of the system. The second order system can be selected as the reference model to meet requirements of settling time, rise time, peak time, and overshoot. Based on

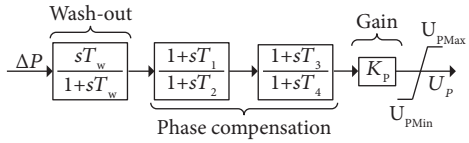

Figure 1: Block diagram of the applied PSS. T_w is the time constant of the straight block, T_1, T_2, T_3, and T_4 are the time constants of the lead and lag blocks, and K_P is the gain of the PSS. The block diagram consists of a wash-out section, a gain section, two phase compensation sections, and a limit section for the output signal.

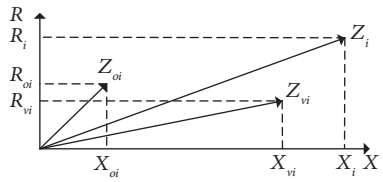

Figure 2: Vector diagram representation of virtual impedance. Z_{vi} is the virtual impedance, Z_{oi} is the PSS output impedance, and Z_i is the PSS-VI output impedance.

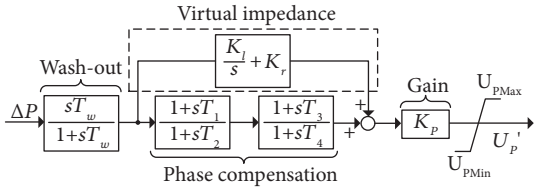

Figure 3: PSS-VI model.

the reference model, general adaptive control laws are established. MRAC contributes greatly to the elimination of modeling errors and dynamic uncertainties. The general block diagram of MRAC is shown in Figure 4.

In this study, based on the general block diagram of MRAC, the reference model is designed by total least squares-estimation of signal parameters via rotational invariance techniques (TLS-ESPRIT) and the regional pole assignment method. Because the proportional integral derivative (PID) controller has a good effect on the elimination of trajectory tracking error, the PID controller is used to eliminate the error between u_p and u_{ref}. The adaptive law is used to adjust the paraments of the PID controller automatically.

2.2.1. Reference Model Design. TLS-ESPRIT is an improved estimation of signal parameters via the rotational invariance techniques (ESPRIT) algorithm proposed by Roy et al. It is a valid identification algorithm to estimate vibration attenuation and sinusoidal signal. In this work, the TLS-ESPRIT algorithm is used for estimating the parameters of signal from the metrical data, which is the angle of the synchronous generator [18, 19].

The process of the TLS-ESPRIT algorithm is as follows:

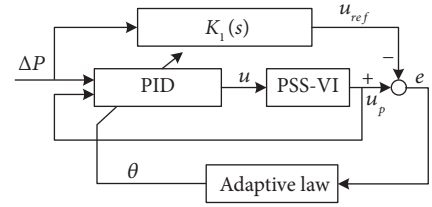

Figure 4: General block diagram of MRAC.

(1) First, LFO signal is sampled, and then, the sampled signal is sorted into a combination of attenuated sinusoidal signal and white noise whose characteristic is the value of amplitude varying exponentially. The mathematical model of the low-frequency oscillation signal is described as follows:

$$x(n) = \sum_{k=1}^{P} a_k e^{j\theta_k} e^{(-\sigma_k + j\omega_k)nT_s} + \omega(n), \tag{1}$$

where P is the equivalent to twice of actual component sine wave, while it also represents the mode order. a_k, θ_k, σ_k, and ω_k, respectively, represent the amplitude, initial phase, attenuation coefficient, and angular frequency of the k^{th} damped sinusoidal quantity. T_s is the sampling period, and $\omega(n)$ is the white Gaussian noise whose average value equals 0.

(2) Then, an appropriate parameter L should be selected. The Hankel matrix H whose order is $L \times M$ can be constructed with preprocessing signals $x_{(n)}$ as follows:

$$H = \begin{bmatrix} x_{(0)} & x_{(1)} & \cdots & x_{(M-1)} \\ x_{(1)} & x_{(2)} & \cdots & x_{(M)} \\ \vdots & \vdots & \vdots & \vdots \\ x_{(L-1)} & x_{(N-L)} & \cdots & x_{(N-1)} \end{bmatrix}, \tag{2}$$

where L is the number of data records, M is the time-window length, and N is the number of the sampling points of low-frequency oscillation signal. Additionally, $L > P$, $M > P$, and $N = L + M - 1$.

(3) Singular value decomposition (SVD) is performed on H. It is divided into a signal subspace and a noise subspace as follows:

$$X = U\Lambda V^H = [\, U_S \;\; U_N \,] \begin{bmatrix} \sum S & 0 \\ 0 & \sum N \end{bmatrix} \begin{bmatrix} V_S^H \\ V_N^H \end{bmatrix}, \tag{3}$$

where the signal space is classified by U and V according to the magnitude of singular values, and the subscripts S and N correspond to the signal subspace and the noise subspace, respectively. The superscript H stands for conjugate transpose, that is to say, $U^H U = I$ and $V^H V = I$. Λ is a diagonal matrix whose diagonal elements are the singular values of matrix X, U is an $L \times L$ unitary matrix, V is an $M \times M$ unitary matrix, and I is the unit diagonal matrix.

(4) Since the signal subspace after SVD has rotation invariance, the signal space is divided into two interwoven subspaces, while there must be reversible diagonal matrix Ψ to make the equation be established.

$$\begin{cases} V_s = \begin{bmatrix} V_1 \\ \vdots \end{bmatrix} = \begin{bmatrix} \vdots \\ V_2 \end{bmatrix}, \\ V_2 = V_1 \Psi \end{cases} \tag{4}$$

where V_1 is the matrix obtained by removing the last row of V_S and V_2 is the matrix obtained by removing the first row of V_S. Then, matrix V' is structured by V_1 and V_2, and matrix V_T is obtained after SVD performed on V':

$$\begin{cases} V' = \begin{bmatrix} V_1 & V_2 \end{bmatrix} \\ V_t = \begin{bmatrix} V_{11} & V_{12} \\ V_{21} & V_{22} \end{bmatrix}, \end{cases} \tag{5}$$

where V_t is divided into four matrix blocks $P \times P$ and $\Psi_{TLS} = -V_{12}V_{22}^{-1}$.

(5) By calculating the eigenvalue λ_k ($k = 1, 2, 3, ..., P$) of the matrix Ψ_{TLS}, the signal frequency f_k, damping factor σ_k, and damping ratio ξ_k can be estimated.

$$\begin{cases} f_k = \dfrac{\arctan\left(\mathrm{Im}\left(\lambda_k\right)/\mathrm{Re}\left(\lambda_k\right)\right)}{2\pi T_s}, \\ \sigma_k = -\ln\left|\lambda_k\right|/T_s, \\ \xi_k = -\dfrac{\sigma_k}{\sqrt{\sigma_k^2 + \left(2\pi f_k\right)^2}}. \end{cases} \tag{6}$$

(6) The amplitude and initial phase angle are acquired through the least squares (LS) method. According to n points,

$$H = \lambda_b \times Y \tag{7}$$

,

where

$$\begin{cases} H = \begin{bmatrix} x_{(0)} & x_{(1)} & L & x_{(N-1)} \end{bmatrix}^T, \\ Y = \begin{bmatrix} Y_{(0)} & Y_{(1)} & L & Y_{(N-1)} \end{bmatrix}^T, \\ \lambda_b = \begin{bmatrix} 1 & 1 & \cdots & 1 \\ \lambda_1 & \lambda_2 & \cdots & \lambda_k \\ \vdots & \vdots & \ddots & \vdots \\ \lambda_1^{N-1} & \lambda_2^{N-1} & \cdots & \lambda_k^{N-1} \end{bmatrix}, \end{cases} \tag{8}$$

and Y can be obtained by the LS method:

$$Y = \left(\lambda_b^H \lambda_b\right)^{-1} \lambda_b^H H. \tag{9}$$

Then, the original amplitude a_k and the initial phase θ_k can be obtained as follows:

$$\begin{cases} a_k = 2\left|Y_k\right|, \\ \theta_k = \arctan\left(\dfrac{\mathrm{Im}\left(Y_k\right)}{\mathrm{Re}\left(Y_k\right)}\right). \end{cases} \tag{10}$$

According to the oscillation frequency band identified by TLS-ESPRIT, a Butterworth bandpass filter is added, with a frequency range of 0.2–2.5 Hz. In the process of identification, a 2% disturbance is added to simulate the small disturbance of the system, and the corresponding eigenvalues are obtained by the algorithm. The system mainly participates in the local oscillation modes of approximately 1.1 Hz and 1.6 Hz, and the damping ratios are low. They all belong to the poorly damped oscillation modes to be suppressed, which are called the main oscillation modes. The system also participates in an interarea mode of approximately 0.5 Hz, where the damping ratio is slightly higher than the local mode. A Butterworth bandpass filter with a frequency range of 0.2–1.7 Hz is added, and these modes are taken as the identification target. Using TLS-ESPRIT for identification again, the 4th-order transfer function $G(s)$ of the system is given in the following equation:

$$G(s) = \frac{-7.32 \times 10^{-5} s^4 - 1.1972 s^3 - 24.9377 s^2 - 29.058 s - 11.5661}{s^4 + 173379.3 s^3 + 6228.2 s^2 + 7814.1 s + 117.4866}. \tag{11}$$

In order to verify the accuracy of the system transfer function after the order reduction, frequency domain analysis is carried out in MATLAB. As shown in Figure 5, the reduced system has similar magnitude and phase response to the original system.

Then, the controller is designed by using the regional pole assignment method to enhance the stability of the system. The transfer function of the designed controller is as follows:

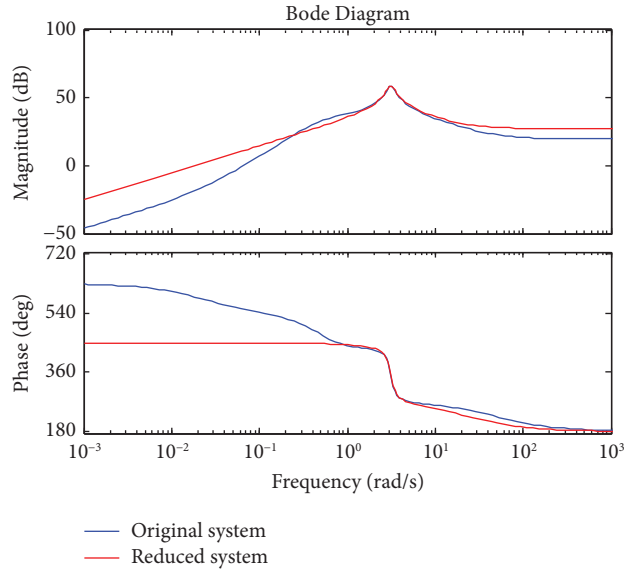

Figure 5: The Bode diagram of system transfer function.

$$K(s) = \frac{-1.16s^5 - 165.31s^4 - 5.44 \times 10^3 s^3 - 4.99 \times 10^4 s^2 - 5.48 \times 10^4 s - 2.11 \times 10^4}{s^6 + 286.29s^5 + 2.85 \times 10^4 s^4 + 1.11 \times 10^6 s^3 + 1.26 \times 10^7 s^2 + 1.73 \times 10^7 s + 2.15 \times 10^5}. \quad (12)$$

It can be seen from equation (12) that the order of the controller obtained is high, which is not conducive to practical application. In this study, the order reduction method of the balanced truncation model based on Hankel SVD is used to reduce the order of the controller. The reduced controller function is as follows:

$$K_1(s) = \frac{-3.26 \times 10^{-9} s - 2.32 \times 10^{-10}}{s^2 + 0.50s + 10.89}. \quad (13)$$

In this study, the obtained controller $K_1(s)$ is designed as the reference model, so that the PSS-VI can output ideal signal. In order to demonstrate the effect of the controller, step response experiment of the system is done in MATLAB. The simulation results are shown in Figure 6, which show that the step response of the system is significantly improved after the design controller is added to the system.

2.2.2. Conventional PID Controller. In the control process, the PID controller is widely used as the reason of simple structure and excellent robustness. Tuning methods are used to improve the performance of PID controllers. Then, the application of PID controllers has grown tremendous. The adopted PID controller in this study is shown in Figure 7.

The consequence of variation of the PID controller is given in Table 1. So, parameter tuning of the PID controller is of great significance to improve its performance. Because the derivative link is too sensitive, the parameters of the differential link are rounded to a very small value to reduce the influence of the differential link on the system.

2.2.3. Adaptive Ratio Controller. Assuming that the system of the controlled object is a linear time invariant system, the default state variable is equal to the output quantity, and the state and output equation can be expressed as

$$\begin{cases} \dot{x}(t) = A_1 x(t) + B_1 u(t), \\ y(t) = x(t). \end{cases} \quad (14)$$

The state and output equation of the reference model is expressed as

$$\begin{cases} \dot{x}_m(t) = A_m x_m(t) + B_m c_m(t), \\ y_m(t) = x_m(t), \end{cases} \quad (15)$$

where $x_m(t)$ is the reference state equation of the reference model, and $c(t)$ is the input signal of the reference model.

First, this work makes a difference between equations (15) and (14):

$$\dot{e}(t) = A_m x_m(t) + B_m c(t) - A_1 x(t) - B_1 u(t), \quad (16)$$

and then, further simplify the following equation:

$$\dot{e}(t) = A_m e(t) + \left[A_m x(t) - A_1 x(t) + B_m c(t) - B_1 u(t)\right], \quad (17)$$

where $e(t) = x_m(t) - x(t)$. If set the error $e(t)$ is equal to 0, the system needs to satisfy that the eigenvalue of the matrix A_m is negative and the output $u(t)$ of the controller of the following equation is as follows:

$$u(t) = ac(t) + bx(t) \quad (18)$$

.

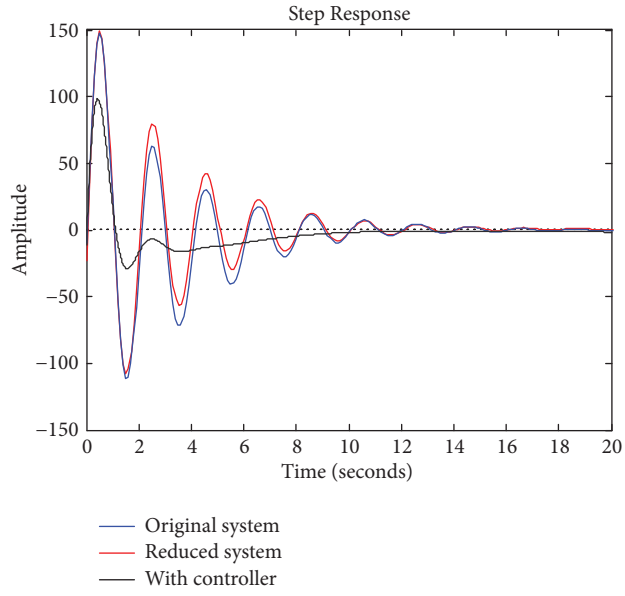

Figure 6: Step response after the controller is connected to the system.

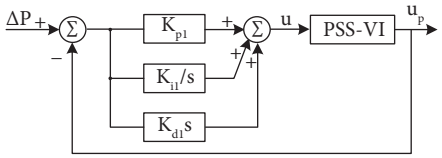

Figure 7: Block of the PID controller. K_{p1}, K_{i1}, and K_{d1} are the parameters of the PID controller.

Table 1: The consequence of parameter variation of the PID controller.

Parameter increase	Rise time	Overshoot	Settling time	Steady state error
K_p	Decreases	Increase	Small change	Decrease
K_i	Decreases	Increase	Increase	Highly reduced
K_d	Small change	Decrease	Decrease	Small change

Therefore, the equation of the controller $u(t)$ can be expressed as equation (18), while parameters a and b are unknown. In a closed-loop system, it should be considered that the controller has only one adjustable parameter θ. The parameter e is defined as the deviation between the output signal (y) of the plant and the output signal (y_m) of the reference model. So, this work adopts the stability theory to calculate a and b.

First of all, the gradient of the state variable deviation of the reference model and the controlled object can be expressed as follows:

$$\dot{e} = \dot{x}_m(t) - \dot{x}(t) \tag{19}$$

.

According to equations (14) and (15), equations (18) and (19) can be simplified as

$$\dot{e}(t) = A_m e(t) + \left[(A_m - A_1 - B_1 b)x(t) + (B_m - B_1 a)c(t)\right]. \tag{20}$$

When the eigenvalue of the matrix A_m is negative and the following equation sets up, the error will converge to zero.

$$\begin{cases} e_1 = A_m - A_1 - B_1 b = 0, \\ e_2 = B_m - B_1 a = 0. \end{cases} \tag{21}$$

When e, e_1, and e_2 converge to zero, the system will be stable. According to the second method of Lyapunov, this work constructs the following scalar function ($V(e, e_1, e_2)$) containing the introduced adaptation gain γ to calculate equation (21).

$$V = \frac{1}{2}\left(e^2 + \frac{1}{B_1\gamma}\left(A_m - A_1 - B_1 b\right) + \frac{1}{B_1\gamma}\left(B_m - B_1 a\right)^2\right) = \frac{1}{2}\left(e^2 + \frac{1}{B_1\gamma}e_1^2 + \frac{1}{B_1\gamma}e_2^2\right). \tag{22}$$

Take the time derivative of this scalar function,

$$\dot{V}\left(e, e_1, e_2\right) = \frac{dV\left(e, e_1, e_2\right)}{dt} = e\frac{de}{dt} + \frac{1}{B_1\gamma}e_1\frac{de_1}{dt} + \frac{1}{B_1\gamma}e_2\frac{de_2}{dt}. \tag{23}$$

Because equation (23) is regarded as a first-order full state equation under the action of zero input, the stabilization point e_x of the system state is

$$\begin{cases} e = 0 \\ e_1 = 0 \\ e_2 = 0 \end{cases} \tag{24}$$

The scalar function V based on equation (24) satisfies that it has a first-order continuous partial derivative with respect to all variables, and it satisfies as follows:

$$\begin{cases} V\left(e, e_1, e_2\right) > 0 \left(e \neq 0, e_1 \neq 0, e_2 \neq 0\right), \\ V\left(0\right) = 0, \\ \dot{V}\left(e, e_1, e_2\right) = \dfrac{dV\left(e, e_1, e_2\right)}{dt} < 0. \end{cases} \tag{25}$$

When the state trajectories of these three state variables all converge at the stabilization point e_x, it means that e, e_1, and e_2 converge to zero. So,

$$\dot{V}\left(e, e_1, e_2\right) = \frac{dV\left(e, e_1, e_2\right)}{dt} < 0 \Rightarrow e = e_1 = e_2 = 0. \tag{26}$$

According to equations (20) and (23), the equation can be simplified as

$$\begin{aligned} \frac{dV\left(e, e_1, e_2\right)}{dt} &= e\frac{de}{dt} + \frac{1}{B_1\gamma}e_1\frac{de}{dt} + \frac{1}{B_1\gamma}e_2\frac{de}{dt}, \\ &= A_m e^2\left(t\right) + \left[A_m - A - B_1 b\left(t\right)\right]e\left(t\right)x\left(t\right) + \left[B_m - B_1 a\left(t\right)\right]e\left(t\right)c\left(t\right) - \frac{e_1}{\gamma}\frac{db\left(t\right)}{dt} - \frac{e_2}{\gamma}\frac{da\left(t\right)}{dt}, \\ &= A_m e^2\left(t\right) + \frac{e_1}{\gamma}\left[\gamma e\left(t\right)x\left(t\right) - \frac{db\left(t\right)}{dt}\right] + \frac{e_2}{\gamma}\left[\gamma e\left(t\right)c\left(t\right) - \frac{da\left(t\right)}{dt}\right]. \end{aligned} \tag{27}$$

Because of $A_m e^2\left(t\right) < 0$, while

$$\begin{cases} \dfrac{db\left(t\right)}{dt} = \gamma e\left(t\right)x\left(t\right), \\ \dfrac{da\left(t\right)}{dt} = \gamma e\left(t\right)c\left(t\right), \end{cases} \tag{28}$$

$\dot{V}\left(e, e_1, e_2\right) < 0$, and e, e_1, and e_2 converge to zero.

The result is

$$\frac{dV\left(e, e_1, e_2\right)}{dt} = A_m e^2\left(t\right). \tag{29}$$

The adjustment rules obtained by the Lyapunov theory are simple and do not require to filter the signal.

So, MRAC based on the second method of Lyapunov could use equation (28) calculating parameters a and b.

The equation (13) can be expressed in the form of state space:

$$\begin{cases} \dot{x}_m\left(t\right) = \begin{bmatrix} 0 & 1 \\ -10.89 & -0.50 \end{bmatrix}x_m\left(t\right) + \begin{bmatrix} 0 \\ 1 \end{bmatrix}c\left(t\right), \\ y_m\left(t\right) = \begin{bmatrix} -2.32 \times 10^{-10} & -3.26 \times 10^{-9} \end{bmatrix}x_m\left(t\right). \end{cases} \tag{30}$$

The transfer function of the PSS-VI is

$$G_1\left(s\right) = K_P\frac{sT_W}{1 + sT_W}\left(\frac{\left(1 + sT_1\right)\left(1 + sT_3\right)}{\left(1 + sT_2\right)\left(1 + sT_4\right)} + K_r + \frac{K_l}{s}\right). \tag{31}$$

In this work, the author selected $K_P = -0.5$, $T_w = 0.02$, $K_r = -1.2$, $K_l = -36$, $T_1 = 0.3$, $T_2 = 0.08$, $T_3 = 0.06$, and $T_4 = 0.3$ to meet the systems requirements for dynamic performance and stability. So, $G_1(s)$ can be rewritten as follows.

$$G_1\left(s\right) = \frac{-0.06s^2 + 19.88s + 0.054}{s^2 + 49.16s + 150.8}. \tag{32}$$

The equation (32) can be rewritten in the form of state space:

$$\begin{cases} \dot{x}\left(t\right) = \begin{bmatrix} 0 & 1 \\ -150.8 & -49.16 \end{bmatrix}x\left(t\right) + \begin{bmatrix} 0 \\ 1 \end{bmatrix}u\left(t\right), \\ y\left(t\right) = \begin{bmatrix} 0.054 & 19.88 \end{bmatrix}x\left(t\right). \end{cases} \tag{33}$$

According to equations (14)–(28), the paraments of the PID controller can be calculated.

3. Power Network Modeling

The power system modeling is the primary task in studying the power system. The dynamic behavior of a power system can be expressed as a sequence of nonlinear differential-algebraic equations (DAEs) involving N_s state variables, x_i,

and N_t input variables, y_i. This behavior may be described by the following equations:

$$\begin{cases} \dot{X} = f(X,U), \\ Y = g(X,U), \end{cases} \tag{34}$$

where $X = [x_1, x_2, \ldots, x_{Ns}]^T, U = [u_1, u_2, \ldots, u_{Nt}]^T$, and $Y = [y_1, y_2, \ldots, y_{No}]^T$.

In this section, we provide the model of a simple interconnected system with the DFIG.

3.1. Mathematical Model of the DFIG. The controller model in the WTG system is shown in Figure 6. The mechanical controller consists of an aerodynamic model, mechanical drive model, and a pitch angle controller. The electrical controller consists of the DFIG and converter model.

3.1.1. Aerodynamic Model. The aerodynamic turbines model captures the wind speed and converts the wind energy into mechanical energy. It follows the energy conservation principle. The electrical power available in the wind is as follows:

$$\begin{aligned} P_{wt} &= 0.5\pi\rho R^2 v_\omega^2 c_p(\lambda), \\ T_m &= \frac{P_{wt}}{\omega_m}, \end{aligned} \tag{35}$$

where ρ is the air density (m^3), v_ω is the wind speed, R is the radius of the turbine (m/sec), and $c_p(\lambda)$ is the coefficient of the power that is the function of the tip speed ratio and pitch angle.

3.1.2. Mechanical Drive Model. The mechanical drive consists of the gearbox which synchronizes the wind turbine and generator. This model is given as

$$\begin{aligned} \frac{d\omega_r}{dt} &= (T_r - K_s\theta_r)(M_r)^{-1}, \\ \frac{d\omega_{wr}}{dt} &= (K_s\theta_r - T_e)(M_{wr})^{-1}, \\ \frac{d\theta_r}{dt} &= \omega_b(\omega_r - \omega_{wt}), \\ M_{wt} &= 2H_{wt}, \\ M_r &= 2H_r, \end{aligned} \tag{36}$$

where H_{wt} and H_r are the wind turbine and generator inertia constant, ω_{wt} and ω_r are the wind turbine and generator speed, respectively, θ_r is the shaft twist angle, ω_b is the reference wind speed, K_s is the shaft stiffness, and T_r is the torque of the generator.

3.1.3. Pitch Angle Controller. To limit the generator' speed up to a maximum value, the pitch angle controller is employed and is expressed as

$$\frac{d\beta}{dx} = (\beta_{\text{ref}} - \beta)(T_\beta)^{-1}, \tag{37}$$

where β is the blade pitch angle, β_{ref} is the pitch angle reference, and T_β is the controller time constant for the pitch control.

3.1.4. DFIG Model. The DFIG scheme is shown in Figure 8 [20]. The stator terminal is directly connected to the local AC power grid, while rotor slip-ring terminal integrated into the same grid via a dual power converter and transformer. The two converters are named rotor side converter (RSC) and grid side converter (GSC), respectively. The wind generator model contains the wind speed model, wind turbine model, mechanical drive model, and DFIG model with its control system.

According to the block diagram of RSC shown in Figure 9, the equation can be written as

$$\begin{aligned} \frac{dx_1}{dt} &= P_{s\_\text{ref}} - P_s, \\ i_{qr\_\text{ref}} &= K_{p1}(P_{s\_\text{ref}} - P_s) + K_{i1}x_1, \\ \frac{dx_2}{dt} &= i_{qr\_\text{ref}} - i_{qr} = K_{p1}(P_{s\_\text{ref}} - P_s) + K_{i1}x_1 - i_{qr}, \\ \frac{dx_3}{dt} &= v_{s\_\text{ref}} - v_s, \\ i_{dr\_\text{ref}} &= K_{p3}(v_{s\_\text{ref}} - v_s) + K_{i3}x_3, \\ \frac{dx_4}{dt} &= i_{dr\_\text{ref}} - i_{dr} = K_{p3}(v_{s\_\text{ref}} - v_s) + K_{i3}x_3 - i_{dr}, \\ v_{qr} &= K_{p2}\left(K_{p1}\Delta P + K_{i1}x_1 - i_{qr}\right) + K_{i2}x_2 + s_r\omega_s L_m i_{ds} + s_r\omega_s L_{rr} i_{qr}, \\ v_{dr} &= K_{p2}\left(K_{p3}\Delta P + K_{i3}x_1 - i_{dr}\right) + K_{i2}x_4 - s_r\omega_s L_m i_{qs} - s_r\omega_s L_{rr} i_{qr}, \end{aligned} \tag{38}$$

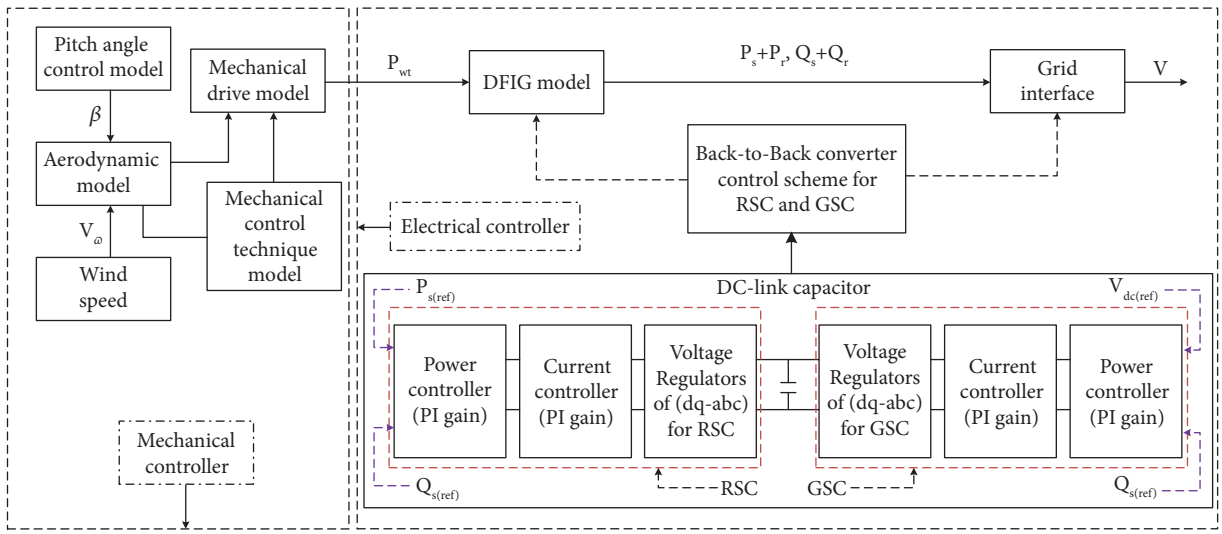

Figure 8: Schematic diagram of the DFIG-based WTG with control scheme and integrated to the grid.

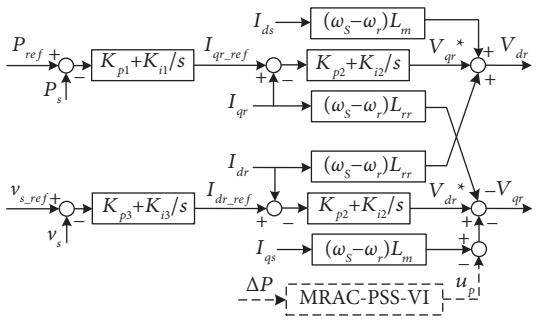

Figure 9: Block diagram of RSC with additional MRAC-PSS-VI.

where K_{p1} and K_{i1} are the proportional and integral coefficients of active power control, respectively, K_{p2} and K_{i2} are the proportional and integral coefficients of current control of RSC, respectively, K_{p3} and K_{i3} are the proportional and integral coefficients of voltage control, respectively, and x_1, x_2, x_3, and x_4 are the intermediate variable of the hypothesis.

It is assumed that the stator and rotor winding are three-phase sinusoidal and symmetrical. The stator and rotor voltage in an arbitrary dq-axis rotating reference frame at a speed of ω_s is expressed as

$$\begin{bmatrix} v_{ds} \\ v_{qs} \\ v_{dr} \\ v_{qr} \end{bmatrix} = \begin{bmatrix} -r_s & (x_s + x_m) & 0 & x_m \\ (x_s + x_m) & -r_s & x_m & 0 \\ 0 & (1-\omega_m)x_m & -r_r & (1-\omega_m)(x_r + x_m) \\ -(1-\omega_m)x_m & 0 & -(1-\omega_m)(x_r + x_m) & -r_r \end{bmatrix} \begin{bmatrix} i_{ds} \\ i_{qs} \\ i_{dr} \\ i_{qr} \end{bmatrix}, \tag{39}$$

where i_{ds}, i_{qs}, and i_{dr}, i_{qr} are the stator and rotor currents in dq-axis; v_{ds}, v_{qs} and v_{dr}, v_{qr} are stator and rotor voltages in dq-axis; x_m is the magnetizing reactance; r_s and x_s are the stator resistance and reactance; r_r and x_r of the rotor resistance and reactance; and ω_m is speed of the rotor.

The stator output active and reactive power delivered to the grid is expressed as

$$[P \;\; Q]^T = [P_s + P_c \;\; Q_s + Q_c]^T \tag{40}$$

.

The stator side output power is

$$\begin{bmatrix} P_s \\ Q_s \end{bmatrix} = \begin{bmatrix} v_{ds} & v_{qs} \\ v_{qs} & -v_{ds} \end{bmatrix} \begin{bmatrix} i_{ds} \\ i_{qs} \end{bmatrix}. \tag{41}$$

On the rotor side, power is given as

$$\begin{bmatrix} P_r \\ Q_r \end{bmatrix} = \begin{bmatrix} v_{dr} & v_{qr} \\ v_{qr} & -v_{dr} \end{bmatrix} \begin{bmatrix} i_{dr} \\ i_{qr} \end{bmatrix}. \tag{42}$$

The grid side converter output power is

$$\begin{bmatrix} P_c \\ Q_c \end{bmatrix} = \begin{bmatrix} v_{dc} & v_{qc} \\ v_{qc} & -v_{dc} \end{bmatrix} \begin{bmatrix} i_{dc} \\ i_{qc} \end{bmatrix}. \tag{43}$$

By neglecting the power losses on GSC,

$$[\,P_c \;\; Q_c\,]^T = [\,P_r \;\; 0\,]^T. \tag{44}$$

Hence, the power delivered to the grid is given as

$$[\,P \;\; Q\,]^T = [\,P_s + P_r \;\; Q_s\,]^T. \tag{45}$$

The generator is modeled as a single shaft as

$$\omega_m = (T_m - T_e)(2H_m)^{-1}, \tag{46}$$

where ω_m is the speed of the rotor, T_e and T_m are the electrical and mechanical torque, respectively, and H_m is inertia of the rotor.

After MRAC-PSS-VI is installed in the RSC loop, the rotor side power is given as

$$\begin{bmatrix} P_r' \\ Q_r' \end{bmatrix} = \begin{bmatrix} v_{dr} & v_{qr} + u_p \\ v_{qr} + u_p & -v_{dr} \end{bmatrix} \begin{bmatrix} i_{dr} \\ i_{qr} \end{bmatrix}. \tag{47}$$

Power delivered to the grid is given again as

$$[\,P' \;\; Q\,]^T = [\,P_s + P_r' \;\; Q_s\,]^T. \tag{48}$$

3.2. Small-Signal Stability Analysis Model. The Lyapunov linearization method is usually used in the stability analysis of small signals. It is proved that the nonlinear system should have characteristics similar to its linearization in sufficiently small motion range [21]. On basis of this, if the real part of all the eigenvalues of A is negative, the system is stable. The dynamic process of the power system can be described by DAEs and can be linearized as

$$\begin{cases} \dot{x} = f(x, y), \\ 0 = g(x, y), \end{cases} \tag{49}$$

where x is the state variable which is used to describe the dynamic characteristics of the system and y is the input vector of the system. In the light of Lyapunov's first law, equation (49) can be linearized as follows at stable operating point (x_0, y_0).

$$\begin{bmatrix} \Delta\dot{x} \\ 0 \end{bmatrix} = \begin{bmatrix} \nabla_x f & \nabla_y f \\ \nabla_x g & \nabla_y g \end{bmatrix} \begin{bmatrix} \Delta x \\ \Delta y \end{bmatrix} = A_C \begin{bmatrix} \Delta x \\ \Delta y \end{bmatrix}, \tag{50}$$

where $\nabla_x f = \partial f(x, y)/\partial x$ is the gradient of the function $f(x, y)$ with respect to x, and other symbols have similar meanings.

Assuming that $\nabla_x f$ is nonsingular, it can be obtained by equation (50) that

$$\Delta\dot{x} = \left[\nabla_x f - \nabla_y f\left(\nabla_y g\right)^{-1} \nabla_x g\right] \Delta x = A\Delta x, \tag{51}$$

where A is the state matrix of the system.

The small-signal stability analysis is mainly to calculate the eigenvalue of A. For the complex eigenvalue $\lambda = \sigma + j\Omega$, the corresponding oscillation frequency is $f = \omega/(2\pi)$, and the corresponding damping ratio is defined as

$$\xi = -\frac{\sigma}{\sqrt{\sigma^2 + \omega^2}}. \tag{52}$$

The participating factor p_{ij} describing the degree of correlation between state variables and modes of the i^{th} state variable for the j^{th} eigenvalue can be calculated by the corresponding left and right eigenvectors v and w, where $p_{ij} = w_{ij} v_{ji} / (w_j^T v_j)$. For any eigenvalue λ_i, the n-dimensional column vectors w_i satisfying $Aw_i = \lambda_i w_i$ $(i = 1, 2, \ldots, n)$ is defined the right eigenvector of λ_i; the n-dimensional row vectors v_i satisfying $v_i A = v_i \lambda_i$ $(i = 1, 2, \ldots, n)$ is defined the left eigenvector of λ_i.

In the small-signal stability analysis of the power system, it is of great significance to study the distribution of eigenvalues on the complex axis. If the real parts of all eigenvalues are negative, the system is stable under small disturbance; if at least one of the real parts of all eigenvalues are positive, the system is unstable under small disturbance; if all eigenvalues have no real part that is positive, but at least one real part is zero, then the system is critically stable.

4. Simulation Results and Analysis

4.1. Test Case Power System Description. In this study, the author adapts the two-area system as the test system. The proverbial two-area system [22] is used for stability analysis to verify the effectiveness of MRAC-PSS-VI on improving power system small-signal stability and transient performance, as shown in Figure 10. In the system, G1–G4 present a group of synchronous generators that are strongly coupled, and both local and interarea oscillation modes are researched. G1 and G2 are equipped with quick excitation, while G3 and G4 are equipped with slow excitation. All the synchronous are equipped with an IEEE (Institute of Electrical and Electronic Engineer) type 1 regulator. The base capacity of the slow excitation system is 100 MVA, the frequency is 50 Hz, and the transmission power of tie line is 400 MW. Regions 1 and 2 of the system are connected by double loop tie lines. G1–G4 are four thermal power generator units whose rated capacity is 900 MVA and rated voltage is 20 kV. The node 3 of the system is the reference node, and the active power output of each generator is 700 MW. The wind farm node is on the area 2 bus 10 (Figure 10). The DFIG was connected to the system via bus 10, and the wind power output is 5 MW.

4.2. Influence of DFIG-MRAC-PSS-VI on Damping Characteristics of the System. It is an appropriate method to evaluate the dynamic stability of the power system by analyzing the damping characteristics of the system, such as damping ratio. In the small-signal stability analysis of the power system, it is significant to study the distribution of eigenvalues on the complex axis. If the real parts of all eigenvalues are negative, the system is stable under small disturbance; if at least one of the real parts of all eigenvalues is positive, the system is unstable under small disturbance; if all eigenvalues have no real part that is positive, but at least one real part is zero, then the system is critically stable.

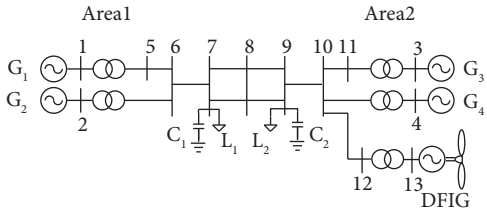

Figure 10: Two-area system.

When the DFIG is connected, the DFIG output is 5 MW, and the original system generator output is not changed. Some eigenvalues of the system are given in Table 2. As given in Table 2, the system has three original oscillation modes: mode 1 and mode 2 represent the local oscillation of the generator sets in region 1 and region 2, respectively, and mode 3 represents the regional oscillation of the generator sets between region 1 and region 2. When the DFIG is connected, an interregional oscillation mode 4 related to the DFIG is added to the system.

Assuming that the load on bus 9 fluctuates upward by 5% during the period of 1.0–1.5 s, the active power emitted by generators G1, G2, and G4 is 700 MW, the DFIG output is 5 MW, and the transmission power of the tie line is 400 MW. Figure 11 shows the voltage curve (unit value) of bus 6 and the angular response curve of generator G1 relative balance node. It can be seen that the response curve without the controller oscillates with a larger amplitude and tends to be stable slowly when the system oscillates at low frequency. When the PSS is installed in the DFIG, the improvement of the response curve is minimal. After the PSS-VI is installed in the DFIG, the power angle curve of generator G1 and the voltage curve of bus 6 decreased, but the effect was not particularly ideal, as shown in Figure 8. However, the response curve with MRAC-PSS-VI has a small amplitude of oscillation and tends to be stable in a short time.

In order to testify the effectiveness of the designed MRAC-PSS-VI controller, this study analyzes the system eigenvalues. It is shown that the power of the system tie line is 400 MW as part of the eigenvalues of the system (Table 3).

As shown in Figure 12, for intraregional oscillation mode 2 and intraregional oscillation mode 4, the eigenvalues of the DFIG with the PSS are slightly shifted to the right, which prove that system damping is reduced. After the addition of the PSS-VI in the DFIG, the eigenvalues for intraregional oscillation mode 2 almost remain unchanged compared with the previous ones, while for interregional oscillation mode 4, the eigenvalues exist a little left shift trend, and the system stability is improved. When the MRAC-PSS-VI controller is installed in the DFIG, the eigenvalues of intraregional oscillation mode 2 and interregional oscillation mode 4 show a large tendency to shift to the left, and the system robustness is significantly improved.

In order to prove the effectiveness of the controller when the system is subjected to different types of perturbations, in this section, it is assumed that a three-phase short circuit fault occurs in the transmission line between bus 6 and bus 7 of the system, and the fault occurs at 1 s, with the duration of 0.01 s and a simulation time of 20 s. Figure 13 shows the power angles of generators G1 and G4, as well as the frequency and voltage curves of bus 9 when the system has a three-phase short circuit fault.

As shown in Figure 13, when faults occur, the power angles of generators G1 and G4 are significantly improved by the addition of MRAC-PSS-VI to the DFIG, while the effects of the addition of the PSS-VI and PSS are not ideal. As shown in Figure 13(c), when low-frequency oscillation occurs in the system, the frequency response curve of bus 9 equipped with the PSS controller oscillates with a larger amplitude and tends to be stable slowly. However, the oscillation amplitude of the response curve is obviously improved and tends to be stable in a short time after the addition of the MRAC-PSS-VI controller. As shown in Figure 13(d), the voltage fluctuation of bus 9 is significantly suppressed after the installation of MRAC-PSS-VI, and the system stability is improved, which is consistent with the results obtained from the above eigenvalue analysis.

4.3. System Simulation of Tie Line Transmission Power Variation. Generator output or load power changes will make the transmission power of the tie line change. Area 1 sends power to area 2. By changing the output of the generators in area 1, the transmission power of tie line is adjusted. In this work, eigenvalues are analyzed for the system in three cases. These cases are as follows:

Case a: the power transmitted on the tie line from region 1 to region 2 is 300 MW

Case b: the power transmitted on the tie line from region 1 to region 2 is 450 MW

Case c: the power transmitted on the tie line from region 1 to region 2 is 600 MW

As given in Table 4, compared with the case of the PSS, the damping characteristics of the system are slightly improved with the addition of the PSS-VI. With the installation of the PSS, the damping ratio of the interregional oscillation mode 4 decreases while the interregional oscillation mode 3 increases slightly. After the addition of the PSS-VI to the system, the damping ratio of the interregional oscillation mode 4 is improved, but the damping ratio of the interregional oscillation mode 3 decreases slightly compared to addition of the PSS to the system. After MRAC-PSS-VI is installed in the DFIG, the damping ratio of interregion oscillation mode 4 and intraregion oscillation mode 2 of the system is greatly improved. For example, in cases a, b, and c, the damping ratio of intraregion oscillation mode 2 increases from 9.154%, 9.921%, and 11.021% to 19.204%, 16.713%, and 17.846%, respectively. The damping ratio of interregion oscillation mode 4 increases from 16.518%, 16.524%, and 16.387% to 28.783%, 29.563%, and 27.713%, respectively, in different cases. Adoption of DFIG-MRAC-PSS-VI further improved the damping characteristics of the system, and the damping ratio of the regional mode was greatly improved, especially the regional mode 4, whose damping ratio was improved by more than 70%. The small disturbance stability of the system is improved, and the system robustness is improved.

Table 2: The eigenvalues of the system.

Mode	Without the DFIG			With the DFIG			Dominant states
	λ	f/Hz	ξ (%)	λ	f/Hz	ξ (%)	
1	$-0.651 \pm j6.547$	1.042	9.898	$-0.651 \pm j6.547$	1.042	9.897	G1, G2
2	$-0.619 \pm j6.392$	1.017	9.645	$-0.620 \pm j6.393$	1.017	9.658	G3, G4
3	$-0.299 \pm j3.135$	0.499	9.526	$-0.300 \pm j3.135$	0.499	9.532	G1–G4
4	—	—	—	$-0.513 \pm j3.059$	0.487	16.539	G1–G4, DFIG

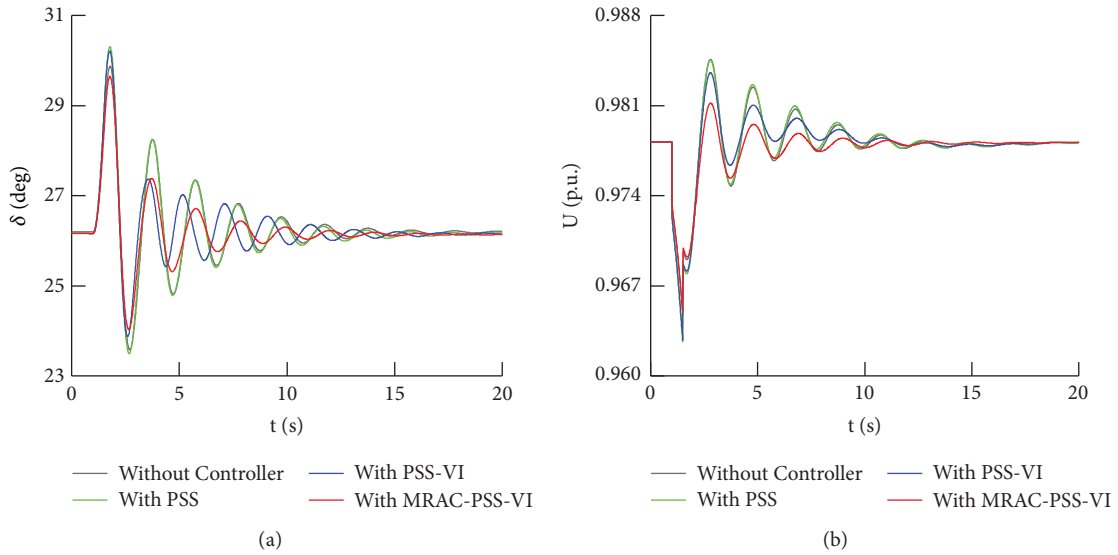

Figure 11: Effects of the MRAC-PSS-VI controller on system damping. (a) Power angle of G1. (b) Voltage of bus 6.

Table 3: The eigenvalues of the system with different controllers.

Mode	Without the controller			With the PSS			Dominant states
	λ	f (Hz)	ξ (%)	λ	f (Hz)	ξ (%)	
1	$-0.651 \pm j6.547$	1.042	9.897	$-0.651 \pm j6.547$	1.042	9.897	G1, G2
2	$-0.620 \pm j6.393$	1.017	9.658	$-0.615 \pm j6.390$	1.017	9.580	G3, G4
3	$-0.300 \pm j3.135$	0.499	9.532	$-0.368 \pm j3.180$	0.506	11.521	G1–G4
4	$-0.513 \pm j3.059$	0.487	16.539	$-0.396 \pm j3.359$	0.535	11.710	G1–G4, DFIG
Mode	With the PSS-VI			With MRAC-PSS-VI			Dominant states
	Λ	f/Hz	ξ (%)	λ	f/Hz	ξ (%)	
1	$-0.651 \pm j6.547$	1.042	9.897	$-0.670 \pm j6.359$	1.012	10.479	G1, G2
2	$-0.620 \pm j6.393$	1.017	9.658	$-1.778 \pm j6.106$	0.972	27.954	G3, G4
3	$-0.298 \pm j3.137$	0.499	9.464	$-0.304 \pm j3.033$	0.483	9.968	G1–G4
4	$-0.689 \pm j3.482$	0.554	19.417	$-0.967 \pm j3.546$	0.564	26.305	G1–G4, DFIG

In this work, the author gives the changes of eigenvalues corresponding to oscillation mode 2 and oscillation mode 4 in case a, as shown in Figure 14.

As shown in Figure 14, after the addition of the PSS in the DFIG, the eigenvalues for intraregional oscillation mode 2 almost remains unchanged compared with the DFIG with the PSS-VI. While for interregional oscillation mode 4 when the PSS-VI is installed in the DFIG, the eigenvalues exist a little left shift trend, and the system stability is improved. While the PSS is installed in the DFIG, the eigenvalues of the system change very little. When the MRAC-PSS-VI controller is installed in the DFIG, the eigenvalues of intraregional oscillation mode 2 and interregional oscillation mode 4 show a large tendency shifting to the left, and the system robustness is significantly improved.

Under the same fault conditions as described in Section 3.1, the system response curves under different tie line powers are shown in Figure 15. It can be seen that with the increase of the power of the tie line, the relative power angle of G1 and G3 gradually increases and the voltage at bus 6 gradually decreases. After the failure, the oscillation amplitude of the curves increased with the increase of the power of the tie line, and the time for the system to stabilize also increased slightly. Under different tie line power conditions,

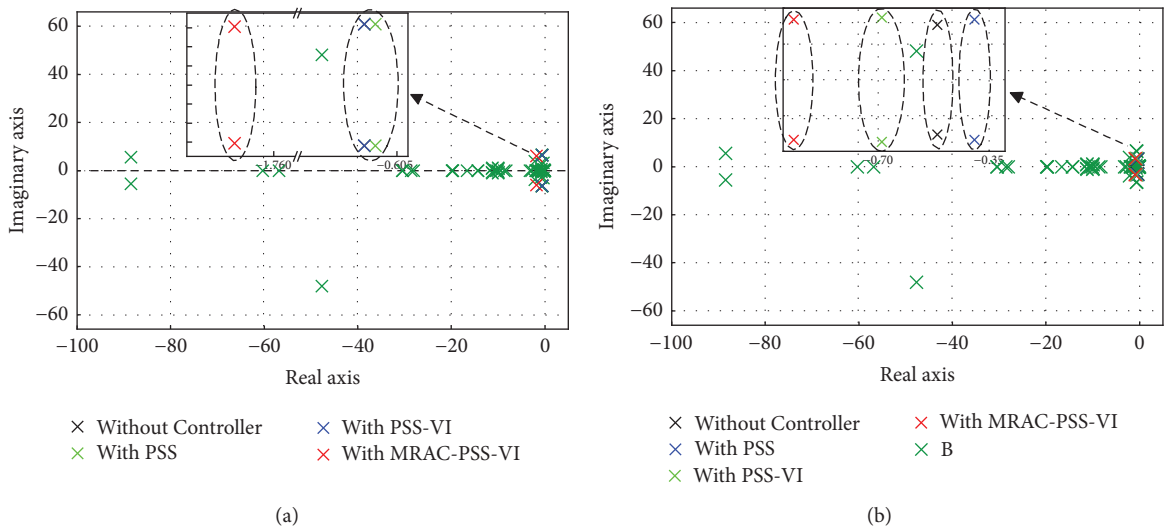

Figure 12: The eigenvalues of the system installed different controllers. (a) Mode 2. (b) Mode 4.

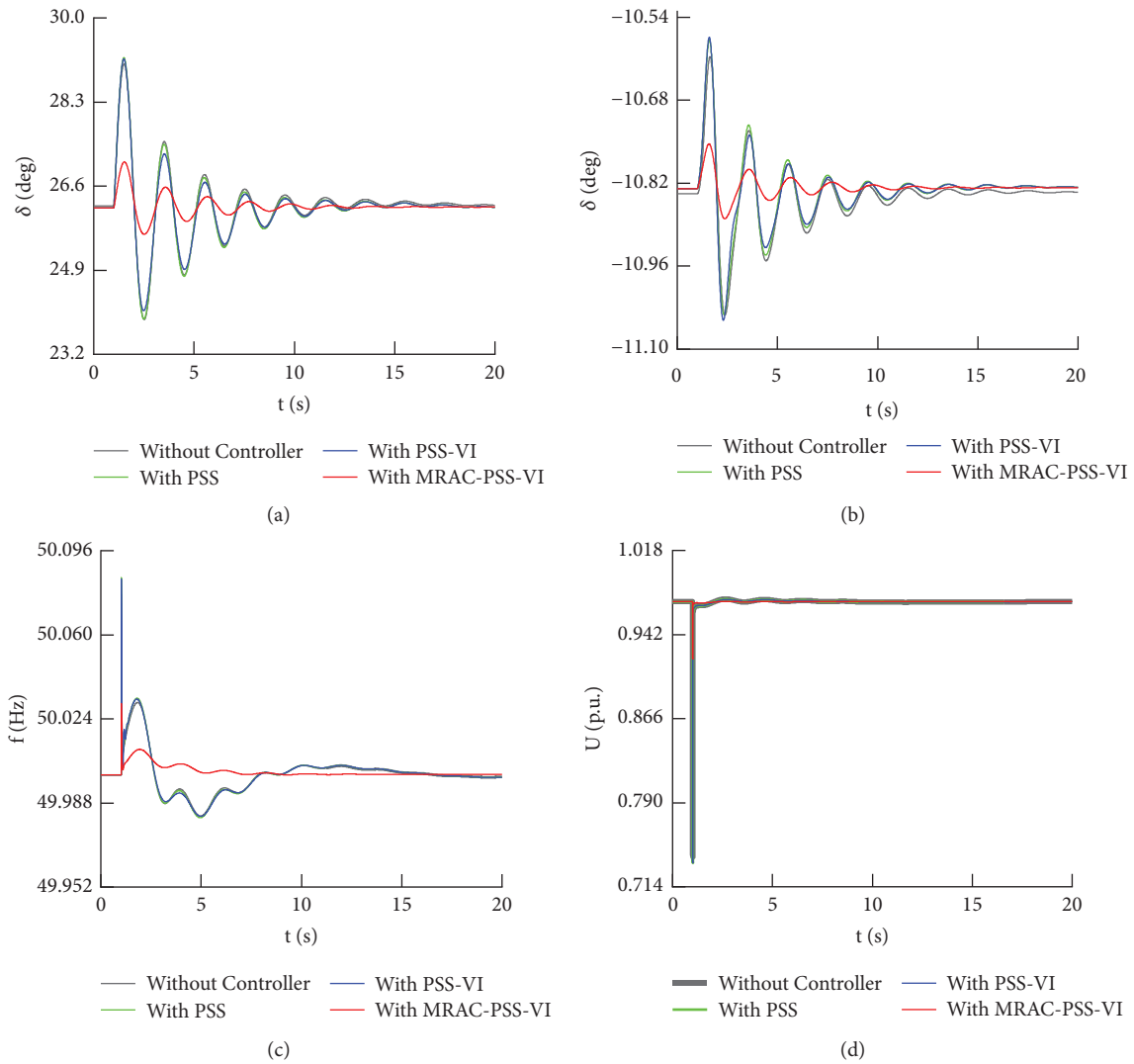

Figure 13: Three-phase short circuit response curve. (a) Power angle of G1. (b) Power angle of G4. (c) Frequency of bus 9. (d) Voltage of bus 9.

Table 4: The eigenvalues of the system in different tie line power conditions.

Mode	Case	Without the controller			PSS			Dominant states
		λ	f (Hz)	ξ (%)	λ	f (Hz)	ξ (%)	
	a	$-0.671 \pm j6.550$	1.042	10.195	$-0.671 \pm j6.550$	1.043	10.196	
1	b	$-0.643 \pm j6.542$	1.041	9.790	$-0.644 \pm j6.542$	1.041	9.789	G1, G2
	c	$-0.618 \pm j6.502$	1.035	9.465	$-0.618 \pm j6.502$	1.034	9.466	
	a	$-0.589 \pm j6.404$	1.019	9.154	$-0.583 \pm j6.401$	1.019	9.079	
2	b	$-0.637 \pm j6.386$	1.016	9.921	$-0.631 \pm j6.383$	1.016	9.839	G3, G4
	c	$-0.704 \pm j6.350$	1.011	11.021	$-0.697 \pm j6.348$	1.010	10.920	
	a	$-0.295 \pm j3.289$	0.524	8.919	$-0.259 \pm j3.293$	0.524	7.827	
3	b	$-0.305 \pm j3.031$	0.482	10.039	$-0.386 \pm j3.055$	0.486	12.539	G1–G4
	c	$-0.343 \pm j2.314$	0.368	14.672	$-0.432 \pm j2.354$	0.375	18.038	
	a	$-0.513 \pm j3.063$	0.488	16.518	$-0.513 \pm j3.407$	0.542	14.877	
4	b	$-0.512 \pm j3.056$	0.486	16.524	$-0.379 \pm j3.379$	0.538	11.159	G1–G4, DFIG
	c	$-0.503 \pm j3.028$	0.482	16.387	$-0.389 \pm j3.390$	0.540	11.412	
Mode	Case	PSS-VI			MRAC-PSS-VI			Dominant states
		λ	f (Hz)	ξ (%)	λ	f (Hz)	ξ (%)	
	a	$-0.671 \pm j6.550$	1.043	10.195	$-0.628 \pm j6.355$	1.011	9.827	
1	b	$-0.644 \pm j6.542$	1.041	9.789	$-0.679 \pm j6.335$	1.008	10.669	G1, G2
	c	$-0.618 \pm j6.502$	1.035	9.464	$-0.746 \pm j6.312$	1.004	11.730	
	a	$-0.589 \pm j6.404$	1.019	9.154	$-1.059 \pm j5.414$	0.862	19.204	
2	b	$-0.637 \pm j6.386$	1.016	9.920	$-0.959 \pm j5.660$	0.901	16.713	G3, G4
	c	$-0.704 \pm j6.350$	1.011	11.021	$-1.153 \pm j6.356$	1.011	17.846	
	a	$-0.293 \pm j3.290$	0.524	8.879	$-0.297 \pm j3.191$	0.508	9.278	
3	b	$-0.304 \pm j3.034$	0.482	9.970	$-0.305 \pm j2.928$	0.466	10.345	G1–G4
	c	$-0.342 \pm j2.321$	0.369	14.589	$-0.332 \pm j2.194$	0.349	14.978	
	a	$-0.687 \pm j3.489$	0.555	19.319	$-1.050 \pm j3.495$	0.556	28.783	
4	b	$-0.689 \pm j3.476$	0.553	19.467	$-1.081 \pm j3.496$	0.556	29.563	G1–G4, DFIG
	c	$-0.689 \pm j3.431$	0.546	19.694	$-0.946 \pm j3.281$	0.522	27.713	

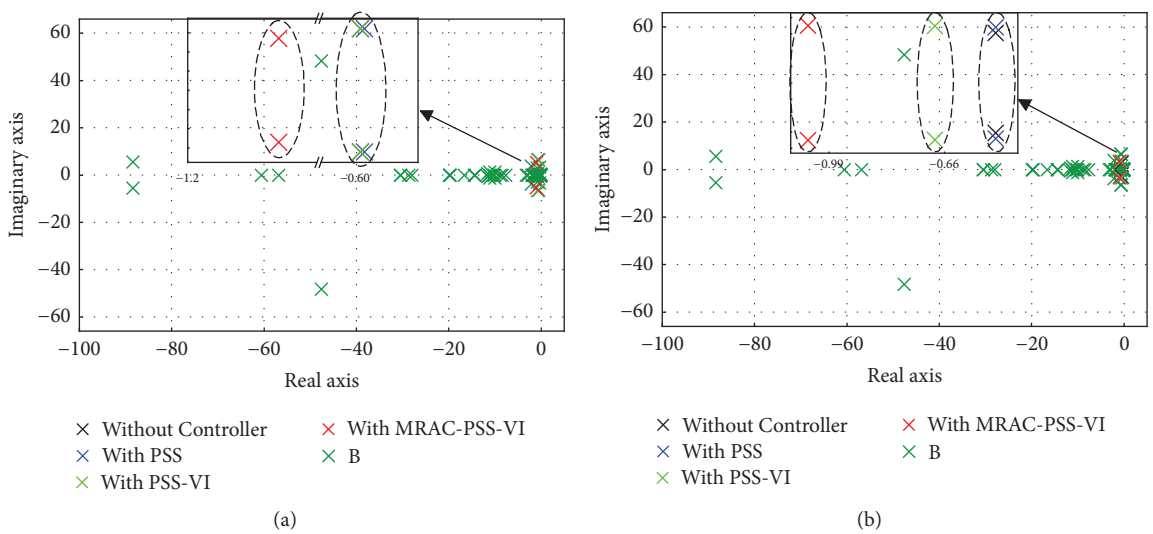

Figure 14: The eigenvalues of the system installed different controllers in case a. (a) Mode 2. (b) Mode 4.

the damping improvement of the DFIG installed the PSS is not obvious. The addition of virtual impedance link to the DFIG-PSS has a certain effect on the stability of the system with small disturbance. Under different tie line power conditions, the power angle curve of G1 and the voltage response curve of bus 6 are improved, but the improvement effect is not ideal in the first cycle. After the MRAC control method is introduced into the DFIG-PSS-VI control, as shown in Figure 12, the power angle curve of G1 and voltage curve of bus 6 are significantly reduced in the case of small interference. The improvement effect of the DFIG with MRAC-PSS-VI is ideal under different tie line power conditions. It can be concluded that after the introduction of the DFIG-MRAC-PSS-VI, the damping of the system is improved and the robustness of the system is significantly improved.

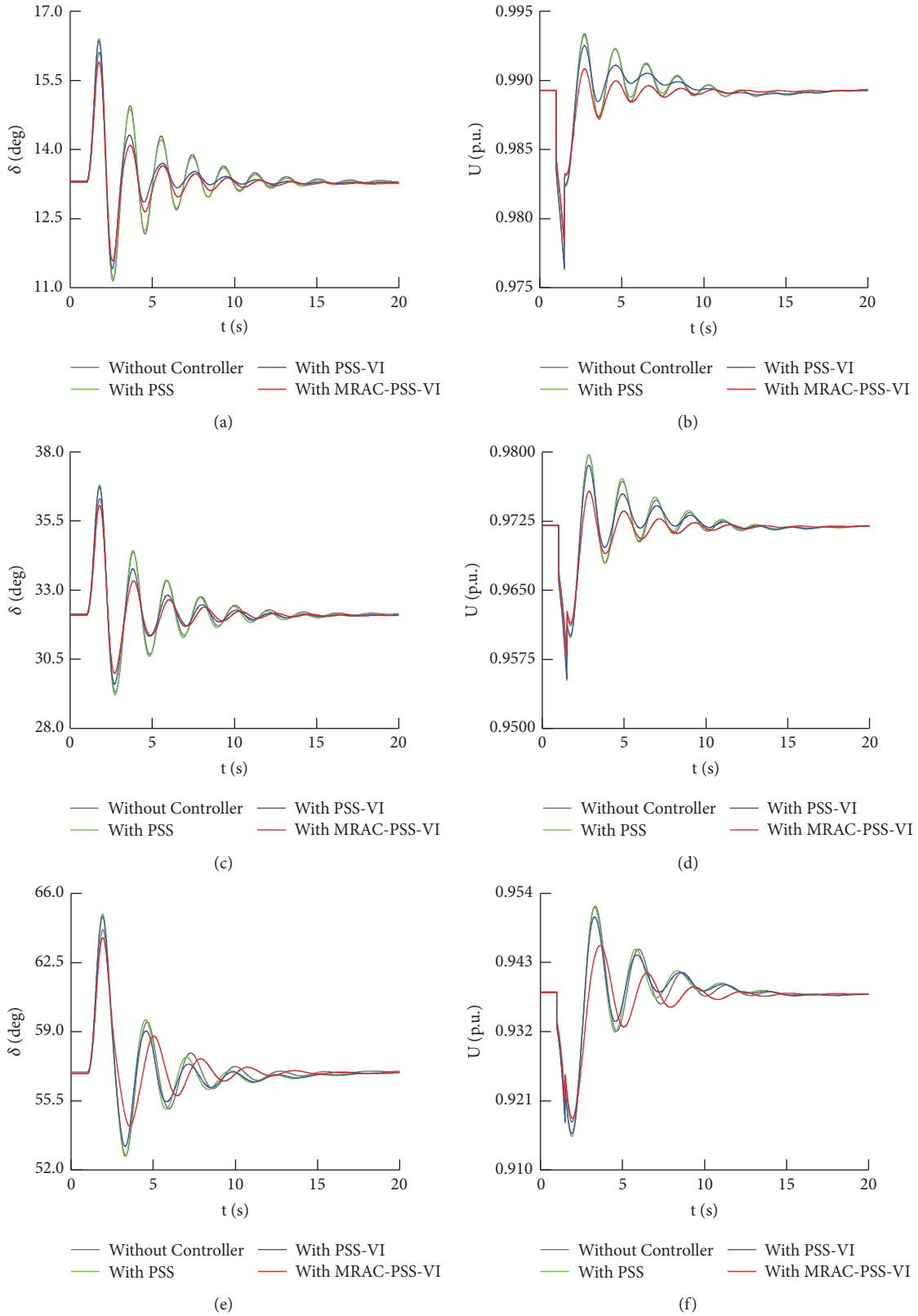

Figure 15: Response curves with different cases under a small disturbance. (a) Power angle of G1 in case a. (b) Voltage of bus 6 in case a. (c) Power angle of G1 in case b. (d) Voltage of bus 6 in case b. (e) Power angle of G1 in case c. (f) Voltage of bus 6 in case c.

Table 5: The eigenvalues of the system in different DFIG access positions.

Mode	Case	Without the controller			PSS			Dominant states
		λ	f (Hz)	ξ (%)	Λ	f (Hz)	ξ (%)	
	d	$-0.652 \pm j6.546$	1.042	9.908	$-0.649 \pm j6.546$	1.042	9.879	
1	e	$-0.651 \pm j6.547$	1.042	9.901	$-0.651 \pm j6.546$	1.042	9.899	G1, G2
	f	$-0.651 \pm j6.547$	1.042	9.896	$-0.651 \pm j6.547$	1.042	9.896	
	d	$-0.620 \pm j6.393$	1.017	9.662	$-0.620 \pm j6.393$	1.017	9.656	
2	e	$-0.621 \pm j6.393$	1.017	9.661	$-0.619 \pm j6.393$	1.017	9.637	G3, G4
	f	$-0.620 \pm j6.393$	1.017	9.654	$-0.616 \pm j6.392$	1.017	9.597	
	d	$-0.303 \pm j3.128$	0.498	9.639	$-0.327 \pm j2.994$	0.476	10.864	
3	e	$-0.302 \pm j3.133$	0.499	9.591	$-0.257 \pm j3.079$	0.490	8.306	G1–G4
	f	$-0.299 \pm j3.137$	0.499	9.500	$-0.290 \pm j3.172$	0.505	9.121	
	d	$-0.807 \pm j3.051$	0.486	25.571	$-0.919 \pm j3.063$	0.487	28.742	
4	e	$-0.791 \pm j3.010$	0.479	25.419	$-0.894 \pm j3.147$	0.501	27.339	G1–G4, DFIG
	f	$-0.807 \pm j3.042$	0.484	25.648	$-0.892 \pm j2.936$	0.467	29.075	
Mode	Case	PSS-VI			MRAC-PSS-VI			Dominant states
		λ	f (Hz)	ξ (%)	λ	f (Hz)	ξ (%)	
	d	$-0.651 \pm j6.545$	1.042	9.892	$-0.760 \pm j6.267$	0.997	12.030	
1	e	$-0.651 \pm j6.547$	1.042	9.902	$-0.668 \pm j6.362$	1.012	10.441	G1, G2
	f	$-0.651 \pm j6.547$	1.042	9.896	$-0.675 \pm j6.351$	1.011	10.563	
	d	$-0.620 \pm j6.393$	1.017	9.658	$-1.057 \pm j6.632$	1.055	15.745	
2	e	$-0.619 \pm j6.392$	1.017	9.645	$-1.426 \pm j5.550$	0.883	24.891	G3, G4
	f	$-0.615 \pm j6.390$	1.017	9.589	$-2.198 \pm j7.205$	1.146	29.187	
	d	$-0.366 \pm j3.187$	0.507	11.405	$-0.307 \pm j3.048$	0.485	10.011	
3	e	$-0.360 \pm j3.140$	0.500	11.385	$-0.303 \pm j3.034$	0.483	9.926	G1–G4
	f	$-0.371 \pm j3.059$	0.487	12.049	$-0.300 \pm j3.036$	0.483	9.829	
	d	$-1.120 \pm j2.927$	0.466	35.749	$-1.421 \pm j3.720$	0.592	35.692	
4	e	$-1.033 \pm j2.844$	0.453	34.144	$-1.187 \pm j3.174$	0.505	35.035	G1–G4, DFIG
	f	$-1.375 \pm j2.814$	0.448	43.911	$-1.225 \pm j3.565$	0.567	32.486	

4.4. System Simulation of DFIG Access Point Changes. The change of the DFIG access position has an impact on the stability of the system. In this section, the controller effect is studied when the DFIG access position is changed. The effectiveness of the designed controller is verified by the following calculation cases:

Case d: DFIG accesses bus 6 in area 1

Case e: DFIG accesses transmission lines 7-8 in area 1

Case f: DFIG accesses bus 9 in area 2

Some oscillation modes of the system after changing the DFIG access position is given in Table 5.

As given in Table 5, the change of the DFIG access point position causes the change of system eigenvalues. For the intraregion oscillation mode 2, the change of system eigenvalue is not obvious after the installation of the PSS and PSS-VI in the DFIG. When the DFIG is in different access positions, the DFIG installed the PSS and PSS-VI has both positive and negative effects on the damping ratio of the system, while the eigenvalue of the MRAC-PSS-VI system shifted significantly to the left, and the damping ratio of the system was greatly improved. For the interregion oscillation mode 4, the damping ratio improvement effect of adding the PSS to the DFIG is limited, while the effect of adding the PSS-VI and MRAC-PSS-VI is more obvious. Although the damping ratio improvement effect of MRAC-PSS-VI is not as good as that of the PSS-VI, the left shift trend of the system characteristic value is obviously better than that of the PSS-VI. In order to further illustrate the effect of the controller, the system is simulated in time domain, and the results are shown in Figure 16.

In this work, the author gives the changes of eigenvalues corresponding to oscillation mode 2 and oscillation mode 4 in case d, as shown in Figure 16.

As shown in Figure 16, after the addition of the PSS and PSS-VI in the DFIG, the eigenvalues for intraregional oscillation mode 2 almost remains unchanged compared with the DFIG without any controller. However, for interregional oscillation mode 4 when the PSS is installed in the DFIG, the eigenvalues exist a little left shift trend, and the system stability is improved. While the PSS-VI is installed in the DFIG, the left shift trend of eigenvalues is bigger than that of the DFIG-PSS. When the MRAC-PSS-VI controller is installed in the DFIG, the eigenvalues of intraregional oscillation mode 2 and interregional oscillation mode 4 show a large tendency shifting to the left, and the system robustness is significantly improved.

In order to verify the effectiveness of the control at different access positions of the DFIG, time domain simulation was carried out. Figure 17 shows the response curves of power angle of G1 and voltage of bus 9.

As shown in Figure 17, the installation of the MRAC-PSS-VI at different access positions of the DFIG has a good effect on system stability. As shown in Figure 17, when the DFIG is equipped with the PSS, the power angle curve oscillation of G1 has no obvious inhibition effect, and the inhibition effect of voltage fluctuation of bus 9 is not obvious either. When the PSS-VI is added, the oscillation is suppressed to some extent, but the effect is not ideal. While the

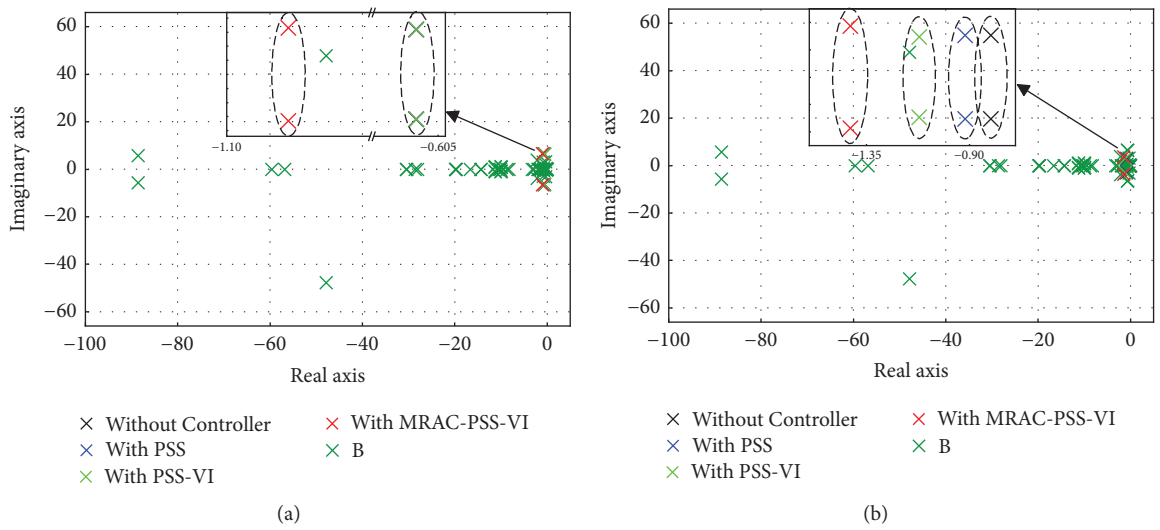

Figure 16: The eigenvalues of system installed different controllers in case d. (a) Mode 2 in case d. (b) Mode 4 in case d.

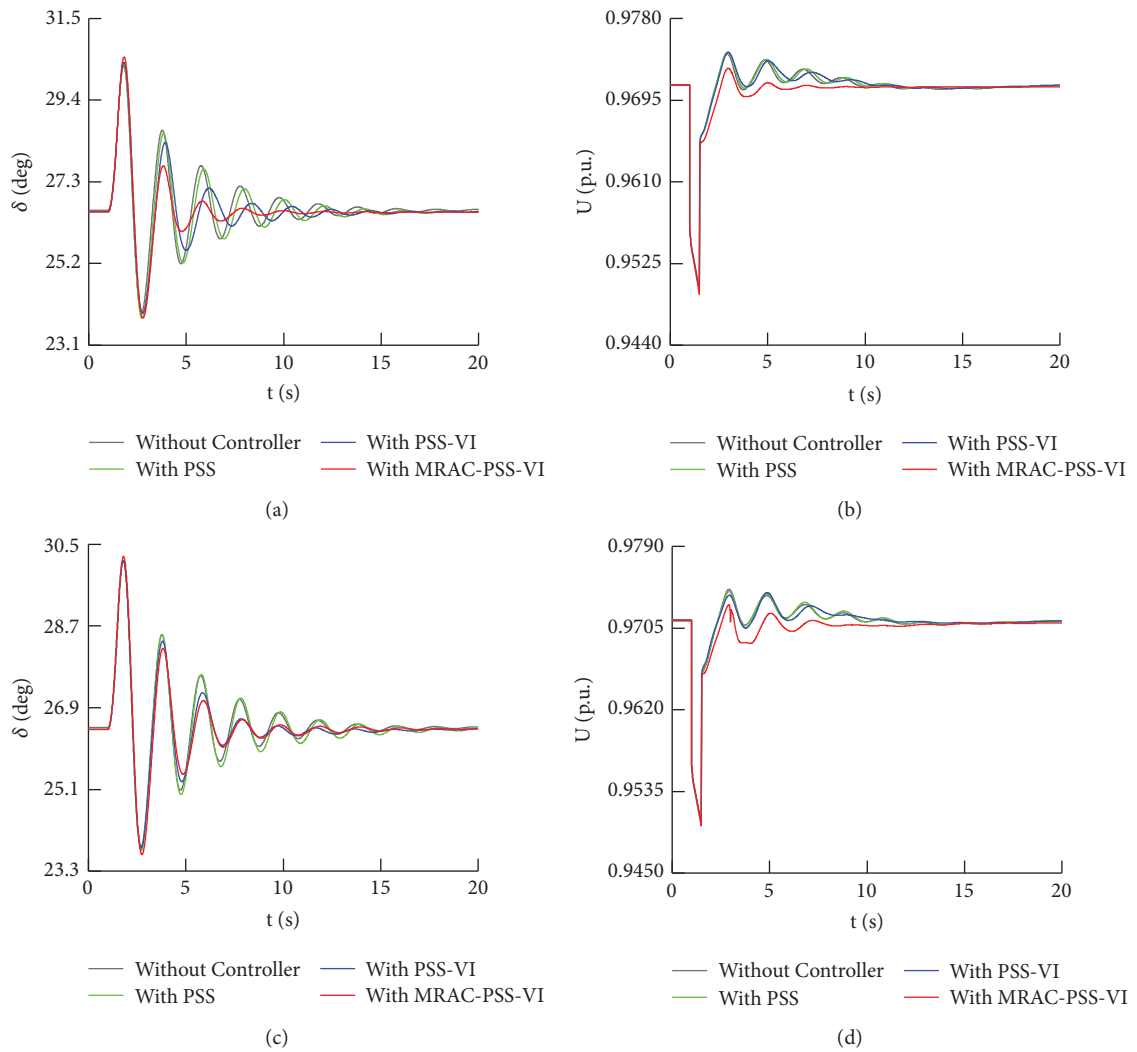

Figure 17: Continued.

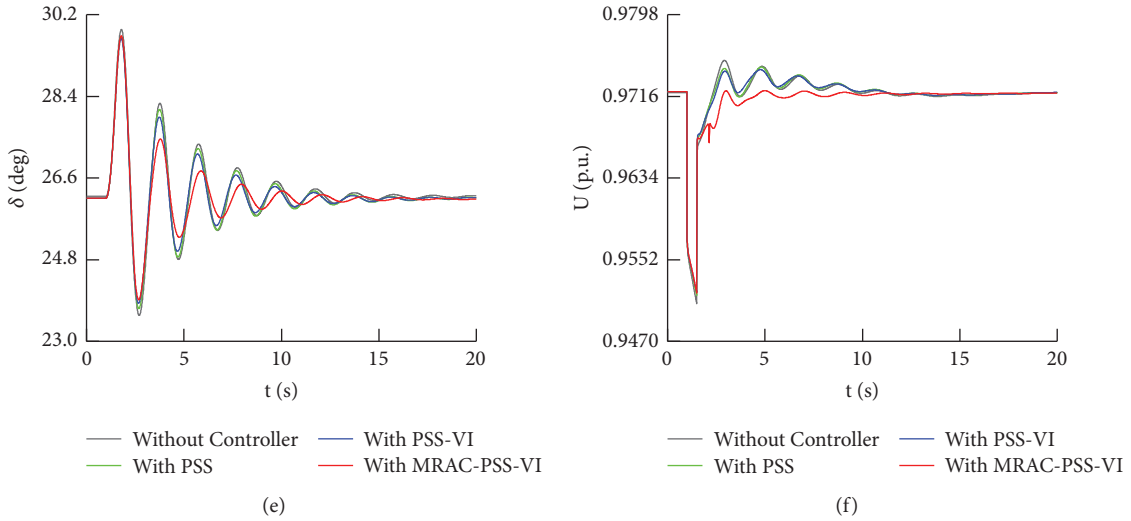

Figure 17: Response curves with different cases. (a) Power angle of G1 in case d. (b) Voltage of bus 9 in case d. (c) Power angle of G1 in case e. (d) Voltage of bus 9 in case e. (e) Power angle of G1 in case f. (f) Voltage of bus 9 in case f.

MRAC-PSS-VI is installed in the DFIG, the oscillation of the system is obviously suppressed, and the rotor angle stability and voltage stability of the system are improved.

5. Conclusion

To solve the low-frequency oscillation problem of the wind power system, this study constructed a MRAC-DFIG-PSS controller based on virtual impedance which was built in DigSILENT/PowerFactory simulation software. This study adopts the 4-machine 2-region system as an example, while the constructed controller was installed into the reactive power control loop of the rotor side controller of the DFIG, and the improvement effect of the designed controller on the low-frequency oscillation characteristics of the system was verified by time domain simulation. The main conclusions are as follows:

(1) The PSS-VI controller whose step response characteristics is better than the traditional controller can improve the stability of the system more obviously

(2) MRAC-PSS-VI installed in the DFIG rotor side reactive power control loop can improve the low-frequency oscillation of the wind power system, and it also has a certain effect when the power of the tie line changes.

(3) The DFIG-MRAC-PSS-VI has a nice influence on system damping whose dominant states contain the DFIG; however, this method only has a little influence on system damping whose dominant states exclude the DFIG.

List of Symbols and Abbreviations:

T_w: The time constant of the straight block
T_1, T_2, T_3, T_4: The time constants of the lead and lag blocks
K_P: The gain of the PSS
Z_{vi}: The virtual impedance
Z_{oi}: The PSS output impedance
Z_i: The PSS-VI output impedance
K_l: The virtual resistance
K_r: The virtual reactance
a_k: The amplitude
θ_k: The initial phase
σ_k: The attenuation coefficient
ω_k: The angular frequency
T_s: The sampling period
$\omega(n)$: The white Gaussian noise
L: The number of data records
M: The time-window length
N: The number of the sampling points of LFO signal
U: The signal space
V: The signal space
Ψ: The reversible diagonal matrix
λ_k: The eigenvalue
f_k: The signal frequency
σ_k: The damping factor
ξ_k: The damping ratio
$G(s)$: The transfer function of the controlled system
$K(s)$: The transfer function of the reference model
K_{p1}, K_{i1}, K_{d1}: The parameters of the PID controller
$x_m(t)$: The reference state equation of the reference model
$c(t)$: The input signal of the reference model
A: The state matrix of the system
γ: The introduced adaptation gain
T_e: The electrical torque
T_m: The mechanical torque
ω_m: The speed of the rotor
ρ: The air density
v_ω: The wind speed

R: The radius of the turbine
$c_p(\lambda)$: The coefficient of the power that is the function of the tip speed ratio and pitch angle
T_r: The torque of the generator
H_{wt}: The wind turbine inertia constant
H_r: The generator inertia constant
ω_{wt}: The wind turbine
ω_r: The generator speed
θ_r: The shaft twist angle
ω_b: The reference wind speed
K_s: The shaft stiffness
β: Blade pitch angle
β_{ref}: The pitch angle reference
T_β: The controller time constant for the pitch control
x_1, x_2, x_3, x_4: The intermediate variables of the hypothesis
P_{s_ref}: The reference output active power of the stator
i_{qr_ref}: The reference current of rotor in q-axis
v_{s_ref}: The reference voltage of the stator
i_{dr_ref}: The reference current of the rotor in d-axis
K_{p1}, K_{i1}: The proportional and integral coefficients of active power control, respectively
K_{p2}, K_{i2}: The proportional and integral coefficients of current control of RSC, respectively
K_{p3}, K_{i3}: The proportional and integral coefficients of voltage control, respectively
P_s: The stator side output active power
Q_s: The stator side output reactive power
i_{ds}, i_{qs}, v_{ds}, v_{qs}: The stator d-axis and q-axis currents and voltage
i_{dr}, i_{qr}, v_{dr}, v_{qr}: The rotor d-axis and q-axis currents and voltage
x_m: The magnetizing reactance
r_s, x_s: The stator resistance and reactance
r_r, x_r: The rotor resistance and reactance.

Data Availability

All data, models, or code that support the findings of this study are available from the corresponding author upon request.

Conflicts of Interest

The authors declare that they have no conflicts of interest.

Acknowledgments

This work was jointly supported by the National Natural Science Foundation of China (NSFC) (51607158), the Scientific and Technological Research Foundation of Henan Province (202102210305), and the Key Project of Zhengzhou University of Light Industry (2020ZDPY0204).

References

[1] R. Pena, J. C. Clare, and G. M. Asher, "Doubly fed induction generator using back-to-back PWM converters and its application to variable-speed wind-energy generation," *IEE Proceedings—Electric Power Applications*, vol. 143, no. 3, pp. 231–241, 1996.

[2] S. A. Gomez and J. L. R. Amenedo, "Grid synchronization of doubly fed induction generators using direct torque control," in *Proceedings of the IEEE 2002 28th Annual Conference of the Industrial Electronics Society*, pp. 3338–3343, Seville, Spain, November 2002.

[3] M. Pichan, H. Rastegar, and M. Monfared, "Two fuzzy-based direct power control strategies for doubly-fed induction generators in wind energy conversion systems," *Energy*, vol. 51, pp. 154–162, 2013.

[4] F. Akel, T. Ghennam, E. M. Berkouk, and M. Laour, "An improved sensorless decoupled power control scheme of grid connected variable speed wind turbine generator," *Energy Conversion and Management*, vol. 78, pp. 584–594, 2014.

[5] A. Ourici, "Double flux orientation control for a doubly fed induction machine," *International Journal of Electrical Power & Energy Systems*, vol. 43, no. 1, pp. 617–620, 2012.

[6] T. Surinkaew and I. Ngamroo, "Coordinated robust control of DFIG wind turbine and PSS for stabilization of power oscillations considering system uncertainties," *IEEE Transactions on Sustainable Energy*, vol. 3, no. 5, pp. 823–833, 2014.

[7] A. H. M. A. Rahim and I. O. Habiballah, "DFIG rotor voltage control for system dynamic performance enhancement," *Electric Power Systems Research*, vol. 81, no. 2, pp. 503–509, 2011.

[8] F. M. Hughes, O. Anaya-Lara, N. Jenkins, and G. Strbac, "A power system stabilizer for DFIG-based wind generation," *IEEE Transactions on Power Systems*, vol. 21, no. 2, pp. 763–772, 2006.

[9] A. Mendonca and J. A. Pecas Lopes, "Simultaneous tuning of power system stabilizers installed in DFIG-based wind generation," in *Proceedings of the IEEE Lausanne Power Tech*, pp. 219–224, Lausanne, Switzerland, July 2007.

[10] E. Mohamed, K. L. Lo, and O. Anaya-Lara, "Impacts of high penetration of DFIG wind turbines on rotor angle stability of power systems," *IEEE Transactions on Sustainable Energy*, vol. 6, no. 3, pp. 759–766, 2015.

[11] T. Surinkaew and I. Ngamroo, "Hierarchical Co-ordinated wide area and local controls of DFIG wind turbine and PSS for robust power oscillation damping," *IEEE Transactions on Sustainable Energy*, vol. 7, no. 3, pp. 943–955, 2016.

[12] Y. Wang, G. Zhou, and X. Li, "A voltage unbalance compensation strategy based on virtual impedance for DGs in island microgrid without sequence component separation," *Electrical Power and Energy Systems*, vol. 127, pp. 1–10, 2021.

[13] M.-D. Pham and H.-H. Lee, "Virtual impedance control scheme to compensate for voltage harmonics with accurate harmonic power sharing in islanded microgrids," *IEEE Transactions on Industrial Electronics*, vol. 68, no. 3, pp. 2279–2288, 2021.

[14] H. Qian, Q. Xu, Y. Xia, J. Zhao, and P. Du, "Analysis and implementation of virtual impedance for fixed-frequency control strategy in microgrid," *IET Generation, Transmission & Distribution*, vol. 15, no. 15, pp. 2262–2276, 2021.

[15] S. Coman and Cr. Boldisor, "Model reference adaptive control for a DC electrical drive," *Bulletin of the Transilvania University of Brasov*, vol. 6, no. 55, pp. 33–38, 2013.

[16] K. Sharma and D. Kumar Palwalia, "A modified PID control with adaptive fuzzy controller applied to DC motor," in *Proceedings of the 2017 International Conference on Information, Communication, Instrumentation and Control (ICICIC)*, Indore, India, August 2017.

[17] M. Vu, I. Stamatescu, C. Dragana, and N. Paraschiv, "Comparison of model reference adaptive control and cascade PID control for ASTank2," in *Proceedings of the 2017 9th IEEE International Conference on Intelligent Data Acquisition and Advanced Computing Systems: Technology and Applications (IDAACS)*, Bucharest, Romania, September 2017.

[18] A. Mohamed, M. Hackl Christoph, and R. Jose, "Model reference adaptive system based sensorless speed estimation of brushless doubly-fed reluctance generator for wind power application," *Energies*, vol. 13, no. 18, pp. 1–15, 2020.

[19] J. Chen, T. Jin, M. A. Mohamed, and M. Wang, "An adaptive TLS-ESPRIT algorithm based on an S-G filter for analysis of low frequency oscillation in wide area measurement systems," *IEEE Access*, vol. 7, pp. 47644–47654, 2019.

[20] J. Bhukya, V. Mahajan, and Vasundhara, "Optimization of damping controller for PSS and SSSC to improve stability of interconnected system with DFIG based wind farm," *International Journal of Electrical Power & Energy Systems*, vol. 108, pp. 314–335, 2019.

[21] L. Rouco, "Eigenvalue-based methods for analysis and control of power system oscillations," in *IEE Colloquium on "Power Dynamics Stabilization"* University of Warwick, Coventry, UK, 1998.

[22] P. Kundur, *Power System Stability and Control*, McGraw-Hill Press, New York, NY, USA, 1994.